

ARTICLE

Open Access

Ultra-small millimeter-wave filter chips based on high-K single-crystal lithium niobate

Qun Li¹, Junyan Zheng¹ and Yansong Yang¹✉

Abstract

Next-generation communication systems require the mass deployment of ultra-small, high-performance filters that integrate multi-physical domains. However, achieving an optimal balance between miniaturization, low insertion loss, high selectivity, and low cost of millimeter-wave filters remains a challenge for existing technologies. Herein, we propose and demonstrate ultra-small millimeter-wave filters based on the multifunctional lithium niobate (LN) with outstanding nonlinear optical, electro-optic, piezoelectric, ferroelectric, and thermoelectric characteristics. As a high-K material with low dielectric loss and straightforward fabrication, LN provides an ideal platform for integrating photonic, acoustic, and electromagnetic functionalities. Notably, while LN is already proven for acoustic and optical signal processing, its potential for electromagnetic signal processing remains largely unexplored. In this work, we introduce second-order and fourth-order LN-based millimeter-wave bandpass filters (BPFs) tailored for narrowband and wideband millimeter-wave applications, respectively. Through careful optimization of the LN thickness, we elevate the cutoff frequencies of high-order modes, enhancing frequency selectivity while maintaining compactness. The LN-based BPFs exhibit record-breaking performance metrics, including minimal insertion loss, high selectivity, and compatibility with microfabrication processes. The LN-based BPFs fulfill the critical demands of millimeter-wave wireless communications, sensing, imaging, and emerging quantum information systems, paving the way for scalable, multi-physical integrated circuits.

Introduction

Lithium niobate (LN, or LiNbO_3) is a multifunctional crystal characterized by its nonlinear optical, electro-optic, piezoelectric, ferroelectric, and thermoelectric properties. Referred to as “the silicon of photonics”, the LN is a promising material for photonics^{1–5} and electro-optics^{6–9}. Additionally, owing to the prominent piezoelectric effect, the LN is extensively applied to acoustic resonators^{10–13}, acoustic filters^{14–17}, piezoelectric micro-machined ultrasonic transducers (PMUT)¹⁸, and sensors¹⁹. From the 2G to 5G sub-6 GHz wireless communication terminals, the piezoelectric acoustic filter chips with small size and high selectivity are dominant. However, the millimeter-wave piezoelectric acoustic filter chips suffer from narrow bandwidth and large insertion loss (IL) due to the limited electromechanical coupling coefficient and low quality factor at millimeter wave.

Therefore, electromagnetic millimeter-wave filter chips are the main solutions for millimeter-wave systems. Existing approaches primarily rely on low-K materials to mitigate loss, but this strategy inherently limits the device size reduction. Therefore, this work proposes to utilize LN for millimeter-wave filters, considering the high-K feature of LN with the properties of low dielectric loss, ease of fabrication, and low cost. Figure 1a illustrates the multi-physical platform of LN for photonics, acoustics, and electromagnetics, while Fig. 1b presents the applications in LN-based millimeter-wave filter chips.

The Shannon theorem highlights the potential of the millimeter-wave spectrum, which offers substantial bandwidth that can increase communication capacity^{20–22}. To support high data rate, low latency, large capacity, and large deployment density in 5G/6G systems, millimeter-wave filters must be not only highly selective but also compact and efficient. However, the low-cost millimeter-wave filter chips with small size and high selectivity are extremely challenging. As larger permittivity leads to larger dielectric loss and conductor loss, current filter designs are primarily

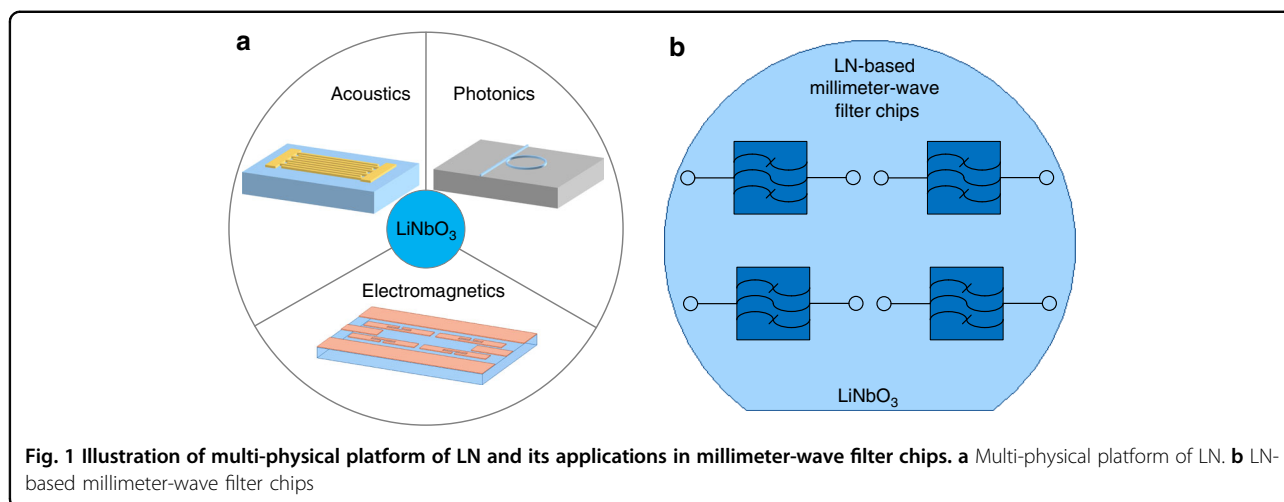
Correspondence: Yansong Yang (eeyyang@ust.hk)

¹Department of Electronic and Computer Engineering, Hong Kong University of Science and Technology, Hong Kong, China

© The Author(s) 2025



Open Access This article is licensed under a Creative Commons Attribution-NonCommercial-NoDerivatives 4.0 International License, which permits any non-commercial use, sharing, distribution and reproduction in any medium or format, as long as you give appropriate credit to the original author(s) and the source, provide a link to the Creative Commons licence, and indicate if you modified the licensed material. You do not have permission under this licence to share adapted material derived from this article or parts of it. The images or other third party material in this article are included in the article's Creative Commons licence, unless indicated otherwise in a credit line to the material. If material is not included in the article's Creative Commons licence and your intended use is not permitted by statutory regulation or exceeds the permitted use, you will need to obtain permission directly from the copyright holder. To view a copy of this licence, visit <http://creativecommons.org/licenses/by-nc-nd/4.0/>.



based on low-K materials and face challenges in achieving miniaturization. The high-K, near-defect-free material is essential to push the boundaries of filter miniaturization while maintaining low losses.

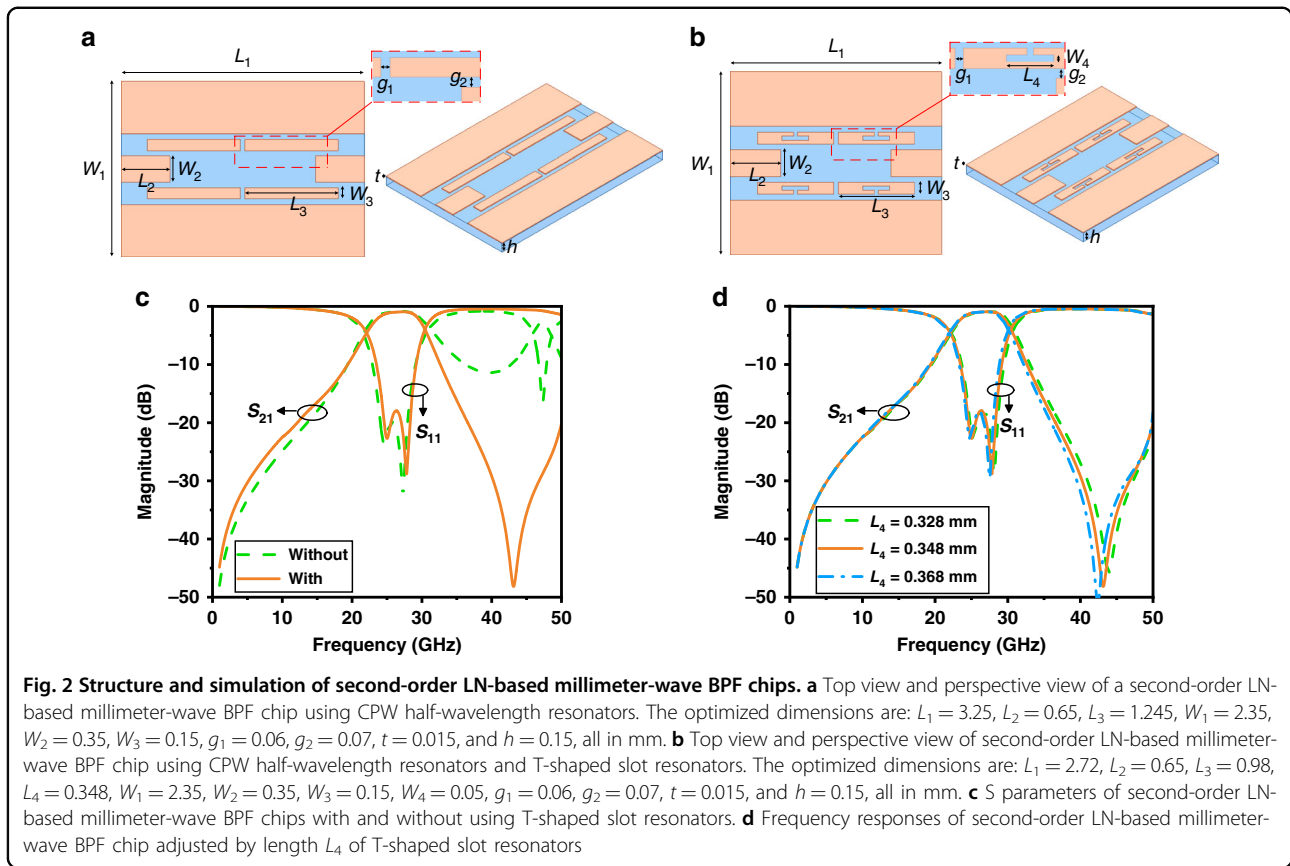
In the past, plenty of millimeter-wave filters have been presented by using the printed circuit board (PCB) process^{23–31}. A microstrip millimeter-wave bandpass filter (BPF) using the PCB process was presented with the center frequency (f_0) of 32 GHz, the measured IL at f_0 of 3.5 dB, and the measured return loss (RL) at f_0 of 10 dB²³. A substrate integrated waveguide (SIW) millimeter-wave BPF using the PCB process was presented with the f_0 of 25.88 GHz, the minimum IL of 4.36 dB, and the size of $0.84 \times 0.53 \lambda_0$ ²⁴. A substrate integrated suspended line (SISL) millimeter-wave BPF using the multi-layer PCB process was presented with the f_0 of 29.2 GHz, the measured IL at f_0 of 1.6 dB, and the fractional bandwidth (FBW) of 10.3%³¹. For the presented millimeter-wave BPF using the PCB process, the fabrication is convenient and cheap, but the filter size and IL are large.

Taking advantage of the multi-layer structure, the low-temperature co-fired ceramic (LTCC) technology has been widely applied to design millimeter-wave BPFs^{32–40}. A SIW millimeter-wave BPF using the LTCC technology was presented with the f_0 of 27.95 GHz, the measured minimum IL of 2.8 dB, and the size of $0.57 \times 0.3 \lambda_0$ ³⁵. A microstrip millimeter-wave BPF using the LTCC technology was presented with the f_0 of 60 GHz, the measured minimum IL of 2.8 dB, FBW of 6.6%, and the size of $0.48 \times 0.206 \lambda_0$ ⁴⁰. For the presented millimeter-wave BPFs using the LTCC technology, the filter size is relatively small, but the IL is large.

Owing to the size reduction and high-precision fabrication, the integrated passive device (IPD) technology is another widely used method to design millimeter-wave BPFs^{41–50}. A millimeter-wave BPF using the 0.1- μm gallium arsenide (GaAs) technology was presented with the

f_0 of 23.5 GHz, the measured minimum IL of 2.9 dB, FBW of 22.2%, and the size of $0.05 \times 0.022 \lambda_0$ ⁴¹. A millimeter-wave BPF using the 130-nm CMOS technology was presented with the f_0 of 34.5 GHz, the measured minimum IL of 1.6 dB, FBW of 61.2%, and the size of $0.03 \times 0.014 \lambda_0$ ⁴⁵. A millimeter-wave BPF using the 130-nm BiCMOS technology was presented with the f_0 of 75.5 GHz, the measured minimum IL of 2.7 dB, FBW of 38.4%, and the size of $0.103 \times 0.044 \lambda_0$ ⁵⁰. Despite the advantage of reduced size, IPD-based millimeter-wave filters typically exhibit high IL. Moreover, the IPD-based millimeter-wave filters are much more expensive than the filters based on PCB and LTCC technologies, which turns out to be an obstacle to mass production.

This article proposes and demonstrates the LN-based millimeter-wave BPF chips with ultra-small size and high selectivity by using the microelectromechanical systems (MEMS) microfabrication technology. Firstly, the coplanar waveguide (CPW) half-wavelength resonators and T-shaped slot resonators are applied to construct a second-order LN-based millimeter-wave BPF chip for narrowband millimeter-wave applications. The T-shaped slot resonators are integrated with the CPW half-wavelength resonators, which can suppress not only the first parasitic passband but also reduce the physical size. Then, the CPW half-wavelength resonators, T-shaped slot resonators, and a CPW dual-mode resonator are applied to construct a fourth-order LN-based millimeter-wave BPF chip for wideband millimeter-wave applications. As a high-K material, the LN-based millimeter-wave BPF chips can realize small sizes but bring the issue of high-order modes, which will deteriorate frequency selectivity. To eliminate the influence of high-order modes, the LN thickness is optimized, and then the cutoff frequencies of the high-order modes are elevated to be far away from the desired passband. The proposed LN-based BPFs exhibit ultra-small size, low passband IL, high selectivity, and



cost-effective production, making them promising candidates for applications in millimeter-wave wireless communications, sensing, imaging, and quantum information systems.

Results and discussion

Second-order LN-based millimeter-wave BPF chip

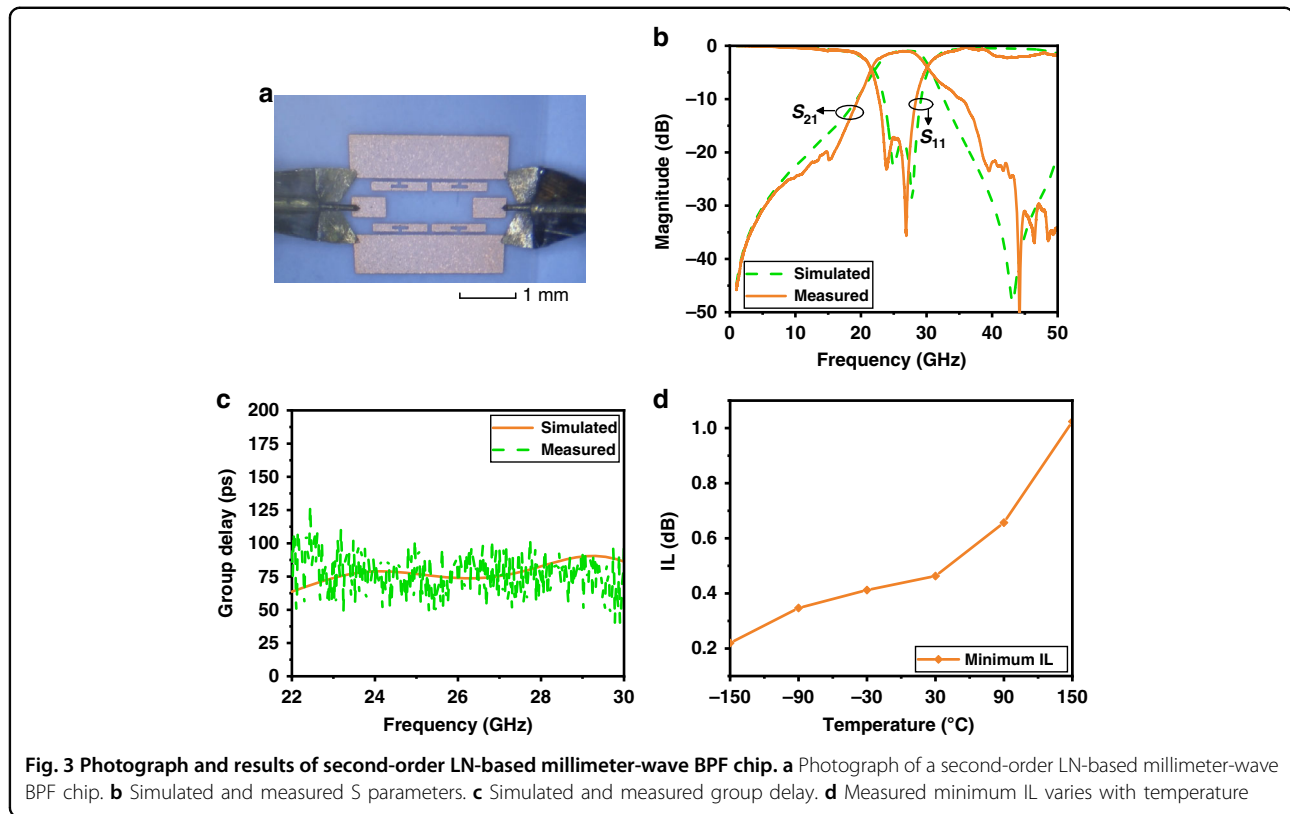
The 128° Y-cut LN with a thickness of 0.15 mm is used herein, and the relative permittivity values are: $\epsilon_{11} = 45$, $\epsilon_{22} = 38.9$, $\epsilon_{33} = 35$. Figure 2a presents the top and perspective views of a second-order LN-based millimeter-wave filter chip using the miniaturized CPW half-wavelength resonators. The f_0 of the passband can be tuned by the resonator length L_3 , while the bandwidth of the passband can be adjusted by the coupling coefficient (K) and the external quality factor (Q_e), which are calculated by

$$K = \frac{f_u^2 - f_l^2}{f_u^2 + f_l^2} \quad (1)$$

$$Q_e = \frac{f_0}{BW_{3dB}} \quad (2)$$

where f_u and f_l represent the upper and lower resonant frequencies, respectively. The coupling scheme of the

second-order LN-based millimeter-wave BPF chip using the CPW half-wavelength resonators is shown in Supplementary Fig. 1a. Based on the coupling principle, the K can be increased by reducing the coupling gap g_1 between two resonators, while the Q_e can be increased by increasing the gap g_2 between the feeding line and the resonator. As a result, the f_0 and bandwidth of the second-order LN-based millimeter-wave filter chip using the CPW half-wavelength resonators can be independently adjusted. However, the parasitic passband occurs at around twice the frequency of the desired passband, which leads to a narrow upper stopband and a low suppression level of the upper stopband. To suppress the first parasitic passband, T-shaped slot resonators are integrated with the CPW half-wavelength resonators. Figure 2b presents the top view and perspective view of the proposed second-order LN-based millimeter-wave BPF chip by using the CPW half-wavelength resonators and T-shaped slot resonators. Each T-shaped slot resonator is equivalent to a capacitor and an inductor connected in parallel, which can create a stopband to suppress the first parasitic passband, resulting in a wide upper stopband and a high suppression level of the upper stopband. The coupling scheme of the second-order LN-based millimeter-wave BPF chip using the CPW half-wavelength resonators and T-shaped slot resonators is



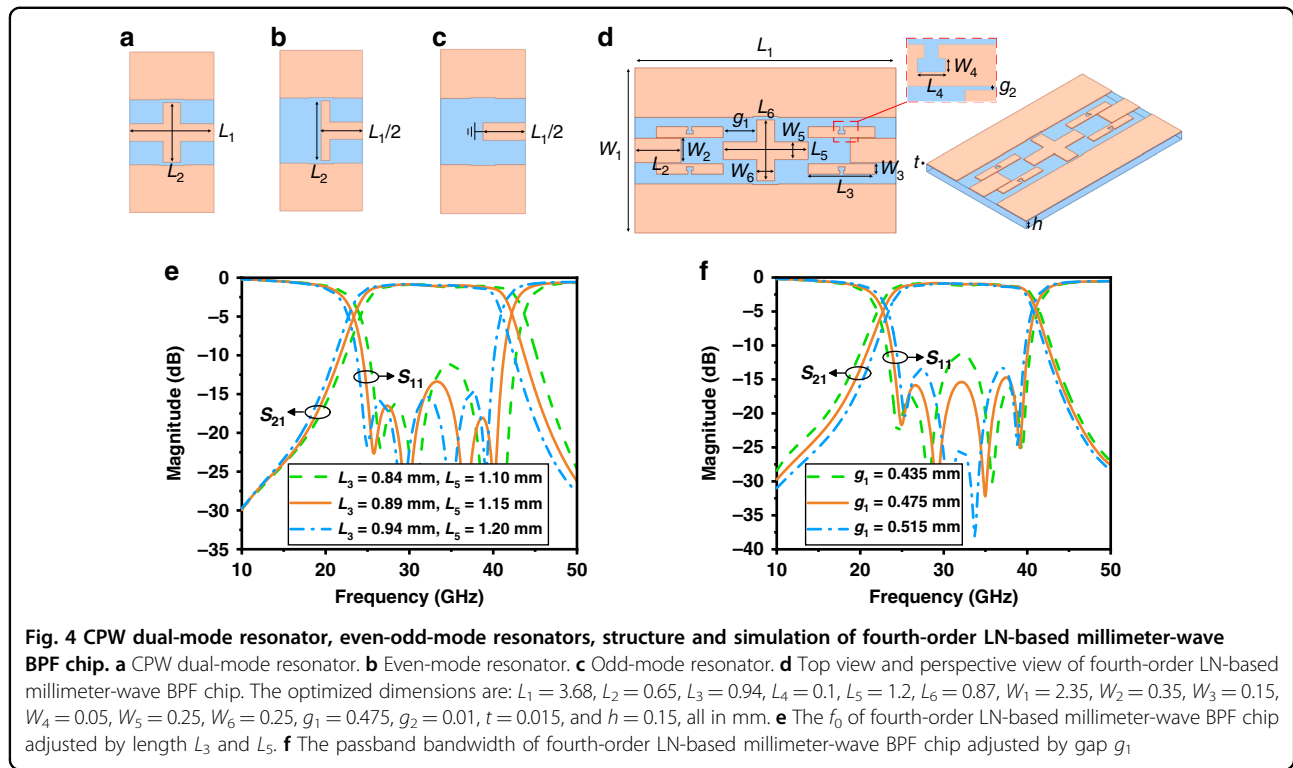
shown in Supplementary Fig. 1b. The f_0 of the second-order LN-based millimeter-wave BPF chip using the CPW half-wavelength resonators and T-shaped slot resonators can be adjusted by the length L_3 as shown in Supplementary Fig. 1c, while the bandwidth can be independently adjusted by the gap g_1 as shown in Supplementary Fig. 1d.

Figure 2c presents the simulated S parameters of the proposed second-order LN-based millimeter-wave BPF chips with and without T-shaped slot resonators. It can be observed that the wide upper stopband and high suppression level are realized by using the T-shaped slot resonators. Figure 2d presents the frequency responses of the second-order LN-based millimeter-wave BPF chip adjusted by the length L_4 of the T-shaped slot resonators. The designed value of the length L_4 is 0.348 mm for the suppression of the first parasitic passband. Moreover, at the f_0 of 26.5 GHz, the length of the CPW half-wavelength resonator is 1.245 mm, while the length of the CPW half-wavelength resonator integrated with a T-shaped slot resonator is 0.98 mm. Thus, the T-shaped slot resonator can not only suppress the first parasitic passband but also reduce the physical size.

Figure 3a presents a photograph of the second-order LN-based millimeter-wave BPF chip using the CPW half-wavelength resonators and T-shaped slot resonators. Two 50-Ohm ground-signal-ground (GSG) probes with a pitch

of 0.6 mm are connected to the CPW feeding line for measurements. The size comparison photograph of the fabricated second-order LN-based millimeter-wave BPF chip with a coin is shown in Supplementary Fig. 2a. Figure 3b presents the simulated and measured S parameters of the fabricated second-order LN-based millimeter-wave BPF chip. The simulated f_0 is 26.5 GHz, and the 3-dB bandwidth is 23–30 GHz (26.4%). The simulated IL and RL at f_0 are 0.97 and 18.04 dB, respectively. From 0 to 12.14 GHz and from 36.57 to 50 GHz, the simulated stopband suppression level (SSL) is over 20 dB. The measured f_0 is 25.85 GHz, and the 3-dB bandwidth is 22.2–29.5 GHz (28.2%), which can cover the n257 and n258 5 G millimeter-wave bands. The measured IL and RL at f_0 are 1.09 and 18.02 dB, respectively. From 0 to 14.57 GHz and from 38.47 to 50 GHz, the measured SSL is over 20 dB. The total chip size is 2.72×2.35 mm, which is equivalent to $0.23 \times 0.2 \lambda_0$, where λ_0 is the free-space wavelength at f_0 of 25.85 GHz. The zoomed-in view of the passband transmission coefficient of the second-order LN-based millimeter-wave BPF chip is shown in Supplementary Fig. 2b.

Figure 3c presents the group delay of the fabricated second-order LN-based millimeter-wave BPF chip. The simulated maximum group delay is 91 ps, while the measured maximum group delay is 129 ps. A cryogenic probe station with a vacuum system and a temperature



control system has been applied for high- and low-temperature measurements. A photograph of the applied cryogenic probe station in the measurement is shown in Supplementary Fig. 3a. Figure 3d presents the measured minimum IL of the fabricated second-order LN-based millimeter-wave BPF chip from -150 °C to 150 °C. It can be observed that the IL is in proportion to the temperature, and the minimum IL at -150 °C is 0.22 dB, which is also a record-breaking value for filtering loss. The measured transmission coefficient and its zoomed-in view at the passband of the fabricated second-order LN-based millimeter-wave BPF chip at -150 °C are shown in Supplementary Fig. 3b. This characterization can reveal the potential of the proposed LN-based millimeter-wave BPFs for the low-temperature quantum information.

Fourth-order LN-based millimeter-wave BPF chip

Based on the above second-order LN-based millimeter-wave BPF chip, a CPW dual-mode resonator is added to construct the proposed fourth-order LN-based millimeter-wave BPF chip. Figure 4a presents the whole structure of the CPW dual-mode resonator. By using the even-odd-mode analysis, a CPW half-wavelength resonator, and a CPW quarter-wavelength resonator are obtained at the even mode and odd mode, respectively. Figure 4b, c presents the schematic diagram of CPW half-wavelength resonator at the even mode and the schematic diagram of CPW quarter-wavelength resonator at the odd mode, respectively. The resonant frequency of the CPW quarter-

wavelength resonator at the odd mode can be tuned by the length L_1 , while the resonant frequency of the CPW half-wavelength resonator at the even mode can be independently tuned by the length L_2 .

Figure 4d presents the top view and perspective view of the proposed fourth-order LN-based millimeter-wave BPF chip. The coupling scheme of the fourth-order LN-based millimeter-wave BPF chip is shown in Supplementary Fig. 4. Figure 4e presents the f_0 of the fourth-order LN-based millimeter-wave BPF chip tuned by the lengths L_3 and L_5 . When the lengths L_3 and L_5 are increased, the f_0 is reduced. Figure 4f presents the passband bandwidth of the fourth-order LN-based millimeter-wave BPF chip adjusted by the coupling gap g_1 . When the gap g_1 is increased, the bandwidth of the passband is reduced. As a result, the f_0 and bandwidth of the proposed fourth-order LN-based millimeter-wave BPF chip can be independently controlled.

Figure 5a presents a photograph of the fabricated fourth-order LN-based millimeter-wave BPF chip, and two 50-ohm GSG probes with a pitch of 0.6 mm are connected to the CPW ports for measurements. The size comparison photograph of the fabricated fourth-order LN-based millimeter-wave BPF chip with a coin is shown in Supplementary Fig. 5. Figure 5b presents the simulated and measured S parameters of the fabricated fourth-order LN-based millimeter-wave BPF chip. The simulated f_0 is 32 GHz, and the 3-dB bandwidth is 23.55–40.45 GHz (52.8%). The simulated IL and RL at f_0 are 0.98 and 15.39 dB, respectively. From 0 to 17.16 GHz and from

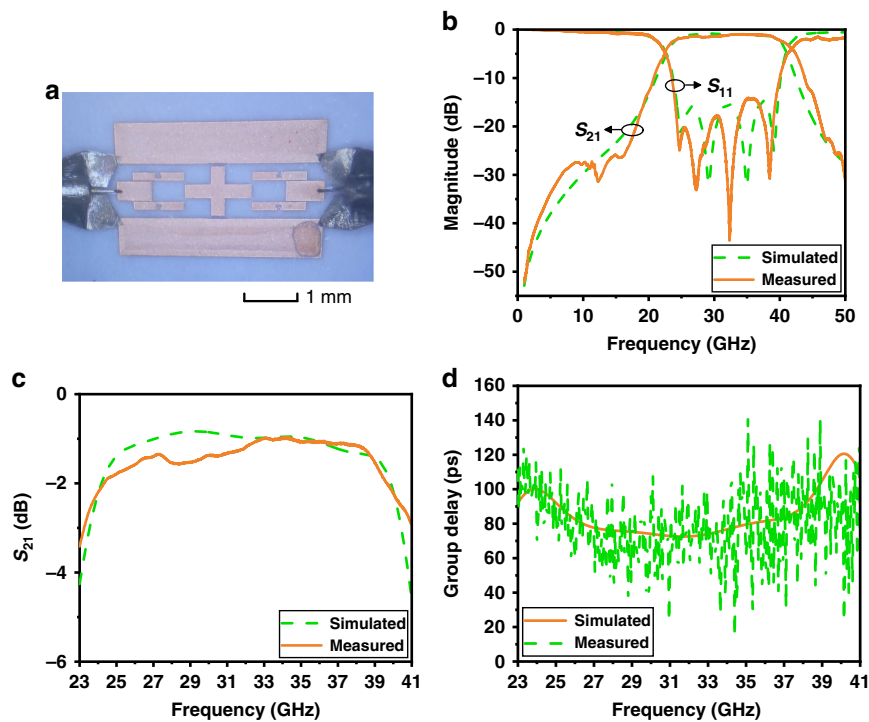


Fig. 5 Photograph and results of fourth-order LN-based millimeter-wave BPF chip. **a** Photograph of a fourth-order LN-based millimeter-wave BPF chip. **b** Simulated and measured S parameters of fourth-order LN-based millimeter-wave BPF chip. **c** Zoomed-in view of transmission coefficient at the passband. **d** Simulated and measured group delay

45.6 to 50 GHz, the simulated SSL is over 20 dB. The measured f_0 is 32.16 GHz, and the 3-dB bandwidth is 23.24–41.08 GHz (55.5%), which can cover the n257, n258, and n260 5 G millimeter-wave bands. The measured IL and RL at f_0 are 1.14 and 35.96 dB, respectively. From 0 to 18.09 GHz and from 46.42 to 50 GHz, the measured SSL is over 20 dB. The total chip size is 3.68×2.35 mm, which is equivalent to $0.39 \times 0.25 \lambda_0$, where λ_0 is the free-space wavelength at f_0 of 32.16 GHz. The zoomed-in view of the transmission coefficient at the passband of the fourth-order LN-based millimeter-wave BPF chip is shown in Fig. 5c. Figure 5d presents the group delay of the fabricated fourth-order LN-based millimeter-wave BPF chip. The simulated maximum group delay is 121 ps, while the measured maximum group delay is 142 ps. Thus, the obtained small group delay of the proposed LN-based millimeter-wave BPFs can fulfill the requirements of high-speed millimeter-wave communications. The fabrication tolerance and copper surface roughness are the main reasons for small discrepancies between simulated and measured results.

Table 1 compares the performance of the presented second-order and fourth-order LN-based millimeter-wave BPF chips with other state-of-the-art millimeter-wave BPFs by using the MEMS, PCB, LTCC, and IPD process technologies. The acoustic millimeter-wave BPFs show small size but

have large IL and small SSL. Generally, the electromagnetic millimeter-wave BPFs based on PCB and LTCC technologies have large size and large IL. The IPD-based millimeter-wave BPFs show small size but have large IL. Moreover, millimeter-wave BPFs based on LTCC and IPD technologies suffer from high cost. It can be observed that our presented second-order and fourth-order LN-based millimeter-wave BPF chips have realized optimal balance among filter size, frequency selectivity, and cost. Our proposed LN-based millimeter-wave BPF chips with ultra-small size, low passband IL, high selectivity, and low cost will be promising for next-generation millimeter-wave wireless communications, sensing, imaging, and quantum information.

Conclusion

The LN crystal film offers a versatile platform that integrates photonic, acoustic, and electromagnetic functionalities. This multifunctionality, combined with its unique properties, makes LN an ideal material for developing high-performance millimeter-wave BPFs. Three critical advantages make LN well-suited for millimeter-wave filter applications. Firstly, as a high-K material, the large permittivity of LN is beneficial for realizing small sizes. Secondly, the LN has a low dielectric loss, which can result in high-Q resonators and high-selectivity filters. Thirdly, the ease of

Table 1 Comparisons with some reported state-of-the-art millimeter-wave BPFs

Ref.	f_0 (GHz)	IL (dB)	FBW (%)	SSL (dB)	Order	Layer	Size ($\lambda_0 \times \lambda_0$)	Platform	Processing
14	23.8	1.52	19.4	12.1	3	4	0.067×0.06	Acoustic Wave	MEMS
17	23.5	2.38	18.2	13	3	3	0.059×0.058	Acoustic Wave	MEMS
23	32	3.5	6.25	20	2	1	NA	Microstrip	PCB
24	25.88	4.36	4.48	20	4	2	0.84×0.53	SIW	PCB
31	29.2	1.6	10.3	20	4	5	NA	SISL	PCB
32	28.5	0.88	14	25	NA	NA	0.24×0.19	NA	LTCC
35	27.95	2.8	3.7	20	4	4	0.57×0.3	SIW	LTCC
40	60	2.8	6.6	20	2	2	0.48×0.206	Microstrip	LTCC
41	23.5	2.9	22.2	20	2	1	0.05×0.022	Microstrip	GaAs
45	34.5	1.6	61.2	20	2	2	0.03×0.014	Microstrip	CMOS
This work	25.85	1.09	28.2	20	2	1	0.23×0.2	CPW	MEMS
	32.16	1.14	55.5	20	4	1	0.39×0.25	CPW	MEMS

fabrication and low cost of LN will facilitate the mass production of our proposed LN-based millimeter-wave BPF chips. Second-order and fourth-order LN-based millimeter-wave BPF chips are presented for narrow-band and wideband millimeter-wave applications, respectively. The fabrication process, which has high production efficiency, a short processing cycle, and low cost, is well suited for mass production of the LN-based millimeter-wave BPF chips. Furthermore, taking advantage of the high-precision MEMS fabrication technology, the working frequency of LN-based filter chips can be extended from the millimeter-wave spectrum to the terahertz-wave spectrum. Our proposed LN-based BPFs fulfill the critical demands of millimeter-wave wireless communications, sensing, imaging, and emerging quantum information systems, paving the way for scalable, multi-physical integrated circuits.

Methods

High-K single-crystal LN

The LN is a high-K single crystal and an anisotropic crystal. The permittivity matrices for any orientations and cuts of LN can be obtained by⁵¹

$$\tilde{\epsilon} = a \cdot \epsilon_Z \cdot a^t \quad (3)$$

Where a is the transformation matrix, and ϵ_Z is the permittivity matrix of Z-cut oriented LN with $\epsilon_{11} = 45$, $\epsilon_{22} = 45$, $\epsilon_{33} = 29$. The high permittivity of LN is critical to realizing the LN-based millimeter-wave filter chips with small sizes. The Czochralski method is applied to produce the single-crystal LN. The ease of fabrication will facilitate the mass production of LN-based millimeter-wave BPF chips.

Cutoff frequency of high-order modes

The high permittivity, thick substrate, and high frequency are three major factors in the excitation of high-order modes, including the transverse magnetic (TM) and transverse electric (TE) modes. The high-order modes in the homogeneous dielectric substrate have been investigated⁵². The cutoff frequencies of high-order modes are expressed as

$$f_c(\text{TM}_n) = \frac{nc}{2h\sqrt{\epsilon_r - 1}} \quad (4)$$

$$f_c(\text{TE}_m) = \frac{(2m - 1)c}{4h\sqrt{\epsilon_r - 1}} \quad (5)$$

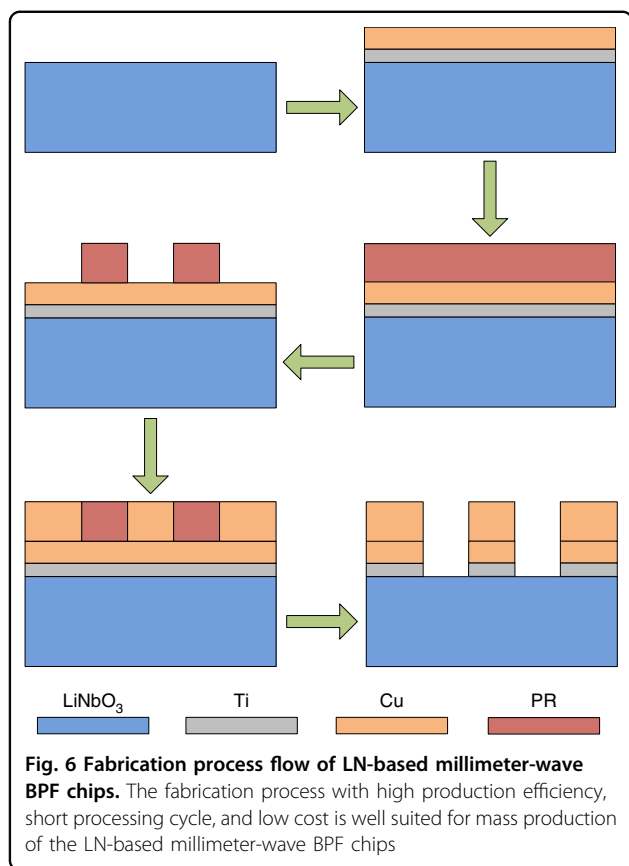
where $n = 0, 2, 4, \dots$ and $m = 1, 3, 5, \dots$ represent the mode order, while the c and h represent the free-space speed of light and the thickness of the substrate, respectively. For the LN with anisotropic permittivity, the above Eqs. (4) and (5) remain valid for analysis. As the TM_0 mode has zero cutoff frequency, the TE_1 mode is the mainly concerned high-order mode.

LN thickness optimization

For the TE_1 mode, the critical height is expressed as

$$h_c(\text{TE}_1) = \frac{c}{4f_c(\text{TE}_1)\sqrt{\epsilon_r - 1}} \quad (6)$$

The cutoff frequency of the TE_1 mode needs to be far away from the desired passband of the proposed LN-based millimeter-wave BPF chips. Here, we let the TE_1



mode have the cutoff frequency of 75 GHz and $\epsilon_r = 45$, and then the calculated critical thickness of LN is 150.8 μm . To increase the cutoff frequency of TE_1 mode, the LN thickness needs to be reduced. However, the reduced LN thickness leads to an increased size of BPF chips. Taking a tradeoff between the cutoff frequency of TE_1 mode and the size, the thickness of the applied 128° Y-cut LN is determined as 150 μm .

Chips fabrication

The MEMS fabrication technology with high precision is applied to fabricate the proposed LN-based millimeter-wave BPF chips. Figure 6 presents the fabrication process flow of our LN-based millimeter-wave BPF chips. Firstly, the 128° Y-cut LN wafer with a thickness of 150 μm and a mask of designed filters are prepared. Secondly, a sputterer is applied to deposit 20-nm titanium as the adhesive layer and then 100-nm copper as the seed layer on one side of the LN wafer. Thirdly, a spin coater is applied to coat a layer of photoresist (PR) with a thickness much larger than the skin depth of copper at the working frequency band. Fourthly, the photolithography is applied to transfer patterns on the PR by using the prepared mask, and then the patterns are created after the development process. Fifthly, considering the intrinsic stress and cost of the sputtered metal, the electroplating of copper is carried

out, and the copper thickness should be much larger than the skin depth of electromagnetic waves.

At the frequency of 30 GHz, the skin depth of copper is 0.38 μm . The thickness of copper without the cover of PR is increased to around the thickness of PR which is much larger than 0.38 μm . Finally, the acetone, copper etchant, and titanium etchant are applied to remove the PR, 100-nm copper seed layer, and 20-nm titanium adhesive layer, respectively. The wet etching of copper can cause lateral etching, but the etching thickness is a little more than 100 nm which is small enough and shall not cause significant performance degradation. The fabrication process, which has high production efficiency, a short processing cycle, and low cost, is well suited for mass production of our proposed LN-based millimeter-wave BPF chips.

Acknowledgements

We acknowledge the Nanosystem Fabrication Facility (CWB) of the Hong Kong University of Science and Technology for the chip fabrication. This work was supported in part by the Hong Kong Research Grants Council under Grant 26202122, in part by the National Natural Science Foundation of China under Grant 62304193, in part by the Hong Kong Innovation and Technology Commission under Grant ITS/144/23, in part by Hong Kong RGC Strategic Topics Grant STG3/E-602/23 N, and in part by HKUST Bridge Gap Fund under Grant BGF.030.2024.

Author contributions

Q.L. and Y.Y. conceived the project. Y.Y. prepared the LN samples. Q.L. and J.Z. fabricated the LN-based millimeter-wave filter chips and performed all the measurements. Q.L., J.Z., and Y.Y. drafted the manuscript. All authors have given approval for the final version of the paper.

Data availability

The data that support the findings of this study are available from the corresponding author on reasonable request.

Conflict of interest

The authors declare no competing interests.

Supplementary information The online version contains supplementary material available at <https://doi.org/10.1038/s41378-025-00947-x>.

Received: 12 December 2024 Revised: 28 February 2025 Accepted: 19 March 2025

Published online: 19 May 2025

References

- Boes, A. et al. Lithium niobate photonics: unlocking the electromagnetic spectrum. *Science* **379**, 1–12 (2023).
- Churaev, M. et al. A heterogeneously integrated lithium niobate-on-silicon nitride photonic platform. *Nat. Commun.* **14**, 3499 (2023).
- Li, Z. et al. High density lithium niobate photonic integrated circuits. *Nat. Commun.* **14**, 4856 (2023).
- Finco, G. et al. Monolithic thin-film lithium niobate broadband spectrometer with one nanometre resolution. *Nat. Commun.* **15**, 2330 (2024).
- Lomonte, E. et al. Single-photon detection and cryogenic reconfigurability in lithium niobate nanophotonic circuits. *Nat. Commun.* **12**, 6847 (2021).
- Xu, Y. et al. Bidirectional interconversion of microwave and light with thin-film lithium niobate. *Nat. Commun.* **12**, 4453 (2021).
- Xu, M. et al. High-performance coherent optical modulators based on thin-film lithium niobate platform. *Nat. Commun.* **11**, 3911 (2020).

8. Yu, M. et al. Integrated electro-optic isolator on thin-film lithium niobate. *Nat. Photonics* **17**, 666–671 (2023).
9. Yu, M. et al. Integrated femtosecond pulse generator on thin-film lithium niobate. *Nature* **612**, 252–258 (2022).
10. Yang, Y., Lu, R., Gao, L. & Gong, S. 10-60-GHz electromechanical resonators using thin-film lithium niobate. *IEEE Trans. Microw. Theory Tech.* **68**, 5211–5220 (2020).
11. Rich, J. et al. Aerosol jet printing of surface acoustic wave microfluidic devices. *Microsyst. Nanoeng.* **10**, 2 (2024).
12. Wang, D., Xie, J., Guo, Y., Shen, M. & Tang, H. X. Noncontact excitation of multi-GHz lithium niobate electromechanical resonators. *Microsyst. Nanoeng.* **10**, 124 (2024).
13. Yang, K. et al. Nanosheet lithium niobate acoustic resonator for mmWave frequencies. *IEEE Electron Device Lett.* **45**, 272–275 (2024).
14. Cho, S. et al. 23.8-GHz acoustic filter in periodically poled piezoelectric film lithium niobate with 1.52-dB IL and 19.4% FBW. *IEEE Microw. Wireless Technol. Lett.* **34**, 391–394 (2024).
15. Cao, X., Wang, C., Li, W. & Cai, Q. An on-chip fractally chipped FBAR filter with Ba-Zn-Fe-Sc-O thin film in 5G-FR2 millimeter-wave band. *IEEE Electron Device Lett.* **44**, 682–685 (2023).
16. Tong, X. et al. 6 GHz lamb wave acoustic filters based on A1-mode lithium niobate thin film resonators with checker-shaped electrodes. *Microsyst. Nanoeng.* **10**, 130 (2024).
17. Barrera, O. et al. Thin-film lithium niobate acoustic filter at 23.5 GHz with 2.38 dB IL and 18.2. *J. Microelectromech. Syst.* **32**, 622–625 (2023).
18. Pop, F., Herrera, B. & Rinaldi, M. Lithium niobate piezoelectric micromachined ultrasonic transducers for high data-rate intrabody communication. *Nat. Commun.* **13**, 1782 (2022).
19. Li, Y. et al. Acoustofluidics-enhanced biosensing with simultaneously high sensitivity and speed. *Microsyst. Nanoeng.* **10**, 92 (2024).
20. Xiao, M. et al. Millimeter wave communications for future mobile networks. *IEEE J. Sel. Areas Commun.* **35**, 1909–1935 (2017).
21. Hong, W. et al. The role of millimeter-wave technologies in 5G/6G wireless communications. *IEEE J. Microw.* **1**, 101–122 (2021).
22. Li, Q., Liao, S., Yang, Y., Liang, Z. & Xiao, S. Wideband 5G millimeter-wave MIMO magnetolectric dipole antenna integrated with partially reflective surfaces. *IEEE Trans. Antennas Propag.* **72**, 445–453 (2024).
23. Hong, S. & Chang, K. Stub-tuned microstrip bandpass filters for millimeter-wave diplexer design. *IEEE Microw. Wirel. Compon. Lett.* **15**, 582–584 (2005).
24. Zhu, L. et al. A design method to realize manufacture-friendly millimeter-wave folded substrate integrated waveguide bandpass filters. *IEEE Trans. Circuits Syst. II Express Briefs* **70**, 979–983 (2023).
25. Yang, X. L., Zhu, X. W., Wang, X. & Hong, W. A general method for implementing flexible filter design based on nested substrate integrated waveguide circular cavity and cambered cavity. *IEEE Trans. Microw. Theory Tech.* **72**, 3637–3649 (2024).
26. Wang, X. et al. Analysis of eighth-mode substrate-integrated waveguide cavity and flexible filter design. *IEEE Trans. Microw. Theory Tech.* **67**, 2701–2712 (2019).
27. Chu, P. et al. Dual-mode substrate integrated waveguide filter with flexible response. *IEEE Trans. Microw. Theory Tech.* **65**, 824–830 (2017).
28. Chan, K. T. et al. High-performance microwave coplanar bandpass and bandstop filters on Si substrates. *IEEE Trans. Microw. Theory Tech.* **51**, 2036–2040 (2003).
29. Aryanfar, F. & Sarabandi, K. Compact millimeter-wave filters using distributed capacitively loaded CPW resonators. *IEEE Trans. Microw. Theory Tech.* **54**, 1161–1165 (2006).
30. Aryanfar, F. & Sarabandi, K. Characterization of semilumped CPW elements for millimeter-wave filter design. *IEEE Trans. Microw. Theory Tech.* **53**, 1288–1293 (2005).
31. Yue, Z., Ma, K. & Wang, Y. Design of Ka-band SISL high selectivity bandpass filter with controllable zeros. *IEEE Microw. Wirel. Technol. Lett.* **33**, 1278–1281 (2023).
32. TDK Electronics. Multilayer band pass filter for 27.5–29.5GHz. MNCB2528G5T-0001A3 datasheet (2019).
33. Wong, S. W., Wang, K., Chen, Z. N. & Chu, Q. X. Electric coupling structure of substrate integrated waveguide (SIW) for the application of 140-GHz Bandpass Filter on LTCC. *IEEE Trans. Compon. Packag. Manuf. Technol.* **4**, 316–322 (2014).
34. Lee, J. H., Pintel, S., Papapolymerou, J., Laskar, J. & Tentzeris, M. M. Low-loss LTCC cavity filters using system-on-package technology at 60 GHz. *IEEE Trans. Microw. Theory Tech.* **53**, 3817–3824 (2005).
35. Chin, K. S. et al. LTCC multilayered substrate-integrated waveguide filter with enhanced frequency selectivity for system-in-package applications. *IEEE Trans. Compon. Packag. Manuf. Technol.* **4**, 664–672 (2014).
36. Wong, S. W., Chen, R. S., Wang, K., Chen, Z. N. & Chu, Q. X. U-shape slots structure on substrate integrated waveguide for 40-GHz bandpass filter using LTCC technology. *IEEE Trans. Compon. Packag. Manuf. Technol.* **5**, 128–134 (2015).
37. Chien, H. Y., Shen, T. M., Huang, T. Y., Wang, W. H. & Wu, R. B. Miniaturized bandpass filters with double-folded substrate integrated waveguide resonators in LTCC. *IEEE Trans. Microw. Theory Tech.* **57**, 1774–1782 (2009).
38. Wang, K. et al. Synthesis method for substrate-integrated waveguide bandpass filter with even-order Chebyshev response. *IEEE Trans. Compon. Packag. Manuf. Technol.* **6**, 126–135 (2016).
39. Wong, S. W., Chen, Z. N. & Chu, Q. X. Microstrip-line millimetre-wave bandpass filter using interdigital coupled-line. *Electron. Lett.* **48**, 224–225 (2012).
40. Guo, Q. Y., Zhang, X. Y., Gao, L., Li, Y. C. & Chen, J. X. Microwave and millimeter-wave LTCC filters using discriminating coupling for mode suppression. *IEEE Trans. Compon. Packag. Manuf. Technol.* **6**, 272–281 (2016).
41. Yang, Y., Zhu, X., Dutkiewicz, E. & Xue, Q. Design of a miniaturized on-chip bandpass filter using edge-coupled resonators for millimeter-wave applications. *IEEE Trans. Electron Devices* **64**, 3822–3828 (2017).
42. Shen, G., Che, W., Feng, W., Shi, Y. & Shen, Y. Low insertion-loss MMIC bandpass filter using lumped-distributed parameters for millimeter-wave application. *IEEE Trans. Compon. Packag. Manuf. Technol.* **11**, 98–108 (2021).
43. Shen, G., Feng, W., Che, W., Shi, Y. & Shen, Y. Millimeter-wave dual-band bandpass filter with large bandwidth ratio using GaAs-based integrated passive device technology. *IEEE Electron Device Lett.* **42**, 493–496 (2021).
44. Yu, H., Wu, Y., Yang, Y. & Wang, W. IPD millimeter-wave bandpass filter chip based on stepped-impedance coupled-line dual-mode resonator for 5G application. *IEEE Trans. Circuits Syst. II Express Briefs* **69**, 4744–4748 (2022).
45. Ge, Z., Chen, L., Gomez-Garcia, R. & Zhu, X. Millimeter-wave wide-band bandpass filter in CMOS technology using a two-layered highpass-type approach with embedded upper stopband. *IEEE Trans. Circuits Syst. II Express Briefs* **68**, 1586–1590 (2021).
46. Gao, L. & Rebeiz, G. M. Wideband bandpass filter for 5G millimeter-wave application in 45-nm CMOS silicon-on-insulator. *IEEE Electron Device Lett.* **42**, 1244–1247 (2021).
47. Hsu, C. Y., Chen, C. Y. & Chuang, H. R. A 60-GHz millimeter-wave bandpass filter using 0.18- μm CMOS technology. *IEEE Electron Device Lett.* **29**, 246–248 (2008).
48. Yeh, L. K., Chen, C. Y. & Chuang, H. R. A millimeter-wave CPW CMOS on-chip bandpass filter using conductor-backed resonators. *IEEE Electron Device Lett.* **31**, 399–401 (2010).
49. Bautista, M. G. et al. Compact millimeter-wave bandpass filters using quasi-lumped elements in 0.13- μm (Bi)-CMOS technology for 5G wireless systems. *IEEE Trans. Microw. Theory Tech.* **67**, 3064–3073 (2019).
50. Liu, Y. & Xu, K. D. Millimeter-wave bandpass filters using on-chip dual-mode resonators in 0.13- μm SiGe BiCMOS technology. *IEEE Trans. Microw. Theory Tech.* **71**, 3650–3660 (2023).
51. Gong, S. & Piazza, G. Design and analysis of lithium-niobate-based high electromechanical coupling RF-MEMS resonators for wideband filtering. *IEEE Trans. Microw. Theory Tech.* **61**, 403–414 (2013).
52. Marcuse, D. *Theory of Dielectric Optical Waveguides* (Academic Press, 1991).